Marchenko multiple elimination of a laboratory example

Zhang, Lele; Slob, Evert

DOI
10.1093/gji/ggaa062

Publication date
2020

Document Version
Final published version

Published in
Geophysical Journal International

Geophysical Journal International

Geophys. J. Int. (2020) **221,** 1138–1144
Advance Access publication 2020 February 03
GJI Marine Geosciences and Applied Geophysics

doi: 10.1093/gji/ggaa062

Marchenko multiple elimination of a laboratory example

Lele Zhang and Evert Slob

Department of Geoscience and Engineering, Delft University of Technology, 2628 *CN Delft, The Netherlands. E-mail: L.Zhang-1@tudelft.nl*

Accepted 2020 January 31. Received 2020 January 17; in original form 2019 April 27

SUMMARY

The Marchenko multiple elimination (MME) scheme is derived from the coupled Marchenko equations. It is proposed for filtering primary reflections with two-way traveltime from the measured acoustic data. The measured acoustic reflection data are used as its own filter and no model information or adaptive subtraction is required to apply the method. The data obtained after MME are better suited for velocity model construction and artefact-free migration than the measured data. We apply the MME scheme to a measured laboratory data set to evaluate the success of the method. The results suggest that the MME scheme can be the appropriate choice when high-quality pre-processing is performed successfully.

Key words: Controlled source seismology; multiple reflection elimination; wave scattering.

INTRODUCTION

The presence of multiple reflections in the measured data set in exploration geophysics can cause errors in velocity model building and lead to artefacts in subsurface images. Many algorithms have been proposed to remove free-surface-related multiple reflections, such as surface-related multiple elimination (Verschuur *et al.* 1992) and estimation of primaries by sparse inversion (van Groenestijn & Verschuur 2009), and both have achieved success for marine and land data. However, less effort has been devoted to the internal multiple reflections and relatively fewer schemes have been proposed to predict and remove them from the measured reflection response.

Internal multiple reflections, scattered multiple times in the subsurface, can be strong enough to cause artefacts in the migration image from marine and land data. Jakubowicz (1998) proposes to predict and attenuate the first-order internal multiple reflections by combining three primary reflections. These primary reflections need to be picked from the measured data. Araújo *et al.* (1994) derive a scheme for internal multiple reflection attenuation from inverse scattering series (ISS), which has been developed in more detail by Weglein *et al.* (1997). Ten Kroode (2002) and Löer *et al.* (2016) modified the ISS scheme with time truncations to attenuate internal multiple reflections in the time domain. The approximate nature of the predicted events implies that adaptive subtraction needs to be implemented to achieve a multiple-attenuated data set (Matson *et al.* 1999; Luo *et al.* 2011; de Melo *et al.* 2014). Alternately, Berkhout & Verschuur (1997) propose to predict and attenuate internal multiple reflections in a layer-stripping fashion. The scheme is called internal multiple elimination (IME) and is derived based on the common-focus-point concept. A macro velocity model is required to create the redatumed data set and a least-squares matching filter with a minimum-energy criterion needs to be implemented for the subtraction of the predicted internal multiple reflections from the measured reflection response. Applying the minimum-energy criterion can lead to removal of primary reflection information.

Van der Neut & Wapenaar (2016) propose a Marchenko multiple elimination (MME) scheme to eliminate internal multiple reflections from the measured acoustic reflection response without adaptive subtraction. It is derived from the coupled Marchenko equations and requires smooth model information to create time truncations. These time truncations are offset dependent because they chose to select a fixed depth level as the basis to derive the scheme. The MME scheme has been modified to remove the need for model information by using an offset independent truncation time that corresponds to an unknown variable depth (Zhang & Staring 2018). Zhang *et al.* (2019a) propose a transmission compensated MME (T-MME) scheme to eliminate internal multiple reflections and to compensate for transmission losses in primary reflections in one step. It is derived from the coupled Marchenko equations with a modified time truncation (Zhang *et al.* 2018). The T-MME scheme has been extended to account for free-surface and internal multiple reflections by Zhang & Slob (2019). This scheme removes free-surface and internal multiple reflections and compensates for transmission losses in primary reflections in one step without any model information or adaptive subtraction. The filters computed in the T-MME scheme for a chosen truncation time can be used as an initial estimate for the filters needed at a later truncation time. This reduces the computational effort by up to an order of magnitude (Zhang & Slob 2020).

In this paper, we apply the MME scheme to a measured laboratory data set to test the performance. The paper is organized as follows. In the Theory section, the formula of the MME scheme is given and briefly discussed. In the Example section, we apply the MME scheme to numerical and laboratory data sets to evaluate the performance for internal multiple reflection elimination. The Discussion section gives a detailed analysis of the performance of MME scheme and we end with conclusions.

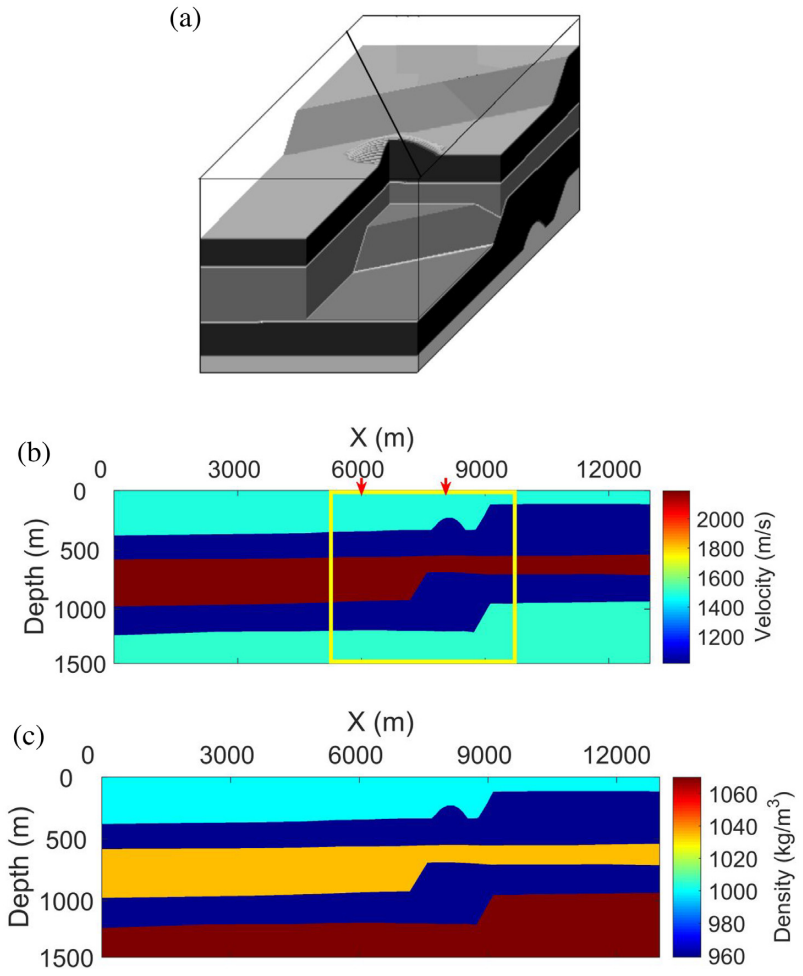

Figure 1. (a) The 3-D physical model. (b) The velocity model of the scaled 2-D cross-section along the acquisition line; the red arrows indicate source positions of two reflection responses shown in Fig. 2, the yellow box marks the target zone that is imaged. (c) The density model of the scaled 2-D cross-section along the acquisition line.

THEORY

We follow Zhang *et al.* (2019b) and give a brief overview of the theory of the MME scheme in this section. The impulse reflection response is denoted as $R(\mathbf{x}'_0, \mathbf{x}_0, t)$ for a source placed at $\mathbf{x}_0$ and receiver placed at $\mathbf{x}'_0$, both at the acquisition surface, and time is denoted as t. The acquisition surface is taken to be acoustically transparent such that free-surface multiple reflections have been removed from $R(\mathbf{x}'_0, \mathbf{x}_0, t)$. The MME scheme can be given as (Zhang *et al.* 2019b)

$$R_t(\mathbf{x}'_0, \mathbf{x}''_0, t) = R(\mathbf{x}'_0, \mathbf{x}''_0, t) + \sum_{m=1}^{\infty} M_m(\mathbf{x}'_0, \mathbf{x}''_0, t) \tag{1}$$

with

$$M_m(\mathbf{x}'_0, \mathbf{x}''_0, t) = (\mathbf{R}\Theta_\tau^{t-\tau}\mathbf{R}^*\Theta_\tau^{t-\tau})M_{m-1}(\mathbf{x}'_0, \mathbf{x}''_0, t), \tag{2}$$

and

$$M_0 = R. \tag{3}$$

In this expression, $\Theta_\tau^{t-\tau}$ is a truncation operator to exclude values outside of the window $(\tau, t-\tau)$ and τ indicates a small positive value; the truncation time window $(\tau, t-\tau)$ is constant for all offsets. The impulse reflection response as a time-convolution and spatial integral operator is denoted as $\mathbf{R}$, while $\mathbf{R}^*$ indicates the same operator in time reverse. All orders of internal multiple reflections are predicted by M_m with $m = 1, ..., \infty$, the retrieved multiple-free data set is denoted as R_t. Eq. (3) is the start of the MME scheme given in eq. (1). The integral form of M_m can be given as

$$\begin{aligned} M_m(\mathbf{x}'_0, \mathbf{x}''_0, t) = &\int_0^{+\infty} \mathrm{d}t' \int_{\partial \mathbf{D}_0} \mathrm{d}\mathbf{x}'''_0 R(\mathbf{x}'_0, \mathbf{x}'''_0, t')H(t-t'-\tau) \\ &\times \int_0^{+\infty} \mathrm{d}t'' \int_{\partial \mathbf{D}_0} \mathrm{d}\mathbf{x}_0 R(\mathbf{x}'''_0, \mathbf{x}_0, t'')H(t'-t''-\tau) \\ &M_{m-1}(\mathbf{x}_0, \mathbf{x}''_0, t-t'+t''), \end{aligned} \tag{4}$$

where H indicates the Heaviside function to impose the truncation time window. Detailed derivation of the MME scheme can be found in Zhang & Staring (2018).

As discussed in Zhang *et al.* (2019b), only the measured reflection response deconvolved for the source wavelet and attenuated for free-surface-related multiple reflections is required for the implementation of the MME scheme. The truncation time t is the time instant at which the equation is evaluated with a constant shift τ. Thus, the scheme presented in eq. (1) is a data-driven scheme and uses only the data for internal multiple reflection elimination.

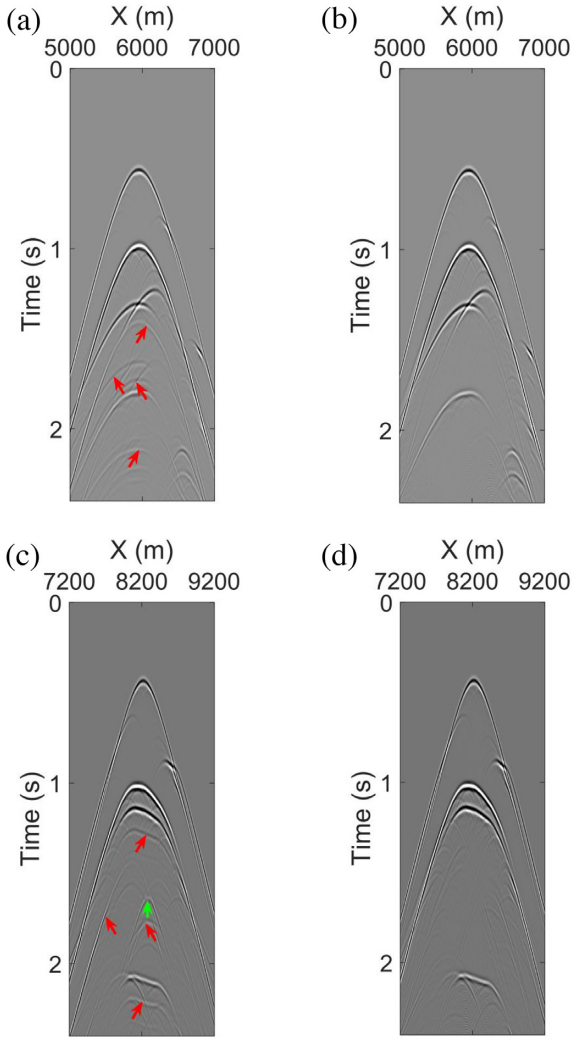

Figure 2. Two computed reflection responses with source positions at 6000 m (a) and 8200 m (c) as indicated by the red arrows in Fig. 1(b), the corresponding retrieved data sets by the MME scheme with source positions at 6000 m (b) and at 8200 m (d). Red and green arrows in (a) and (c) indicate internal multiple reflections.

EXAMPLE

In this section, a laboratory data set acquired with a 3-D geometry from a 3-D physical model shown in Fig. 1(a) is considered. The size of the model is $70 \times 600 \times 600$ mm^3. The model is composed of silicone gel and beeswax layers and is placed in a water tank. The acquisition is carried out along the horizontal line indicated in Fig. 1(a) and the acquisition line is almost perpendicular to the main fault plane of the model. The ultrasonic signal with central frequency 1.1 MHz is emitted and received by piezo-electric transducers 12 mm above the upper boundary of the model. The spacing of the transducers is 1.25 mm. A 2-D cross-section of the model below the acquisition line is shown in Figs 1(b) (velocity) and (c) (density). The spatial dimensions have been scaled by the factor 20 000. A more detailed description of the physical modelling tank and the 3-D acquisition system can be found in Koek *et al.* (1995), Blacquiere *et al.* (1999) and Wapenaar *et al.* (2018). The recording data from the acquisition line is selected as a 2-D experiment to test the performance of the MME scheme. There are 301 shot gathers in the selected 2-D slice and each shot gather has 212 traces. The 2-D numerical data computed from the model shown in Figs 1(b) and (c) are used as a reference to understand the performance of the MME scheme on the measured laboratory data. Note that the 2-D numerical data are computed at the exploration scale, while the laboratory data were measured at the reduced scale and were scaled as an exploration case study in this paper.

Numerical 2-D data set

We compute a 2-D data set from the model shown in Figs 1(b) and (c) with sources and receivers positioned at the top of the model to test the success of the MME scheme. There are 301 shot gathers in the computed 2-D data set and 424 traces per shot gather. The spacing of sources and receivers is 12.5 m. The sources emit a Ricker wavelet with 20 Hz centre frequency. Absorbing boundary conditions are applied around the model such that there are no free-surface multiple reflections present in the computed data. The direct wave has been removed from the computed data. Figs 2(a) and (c) show two of the computed reflection responses with source positions indicated by the red arrows (6000 and 8200 m) in Fig. 1(b). Internal multiple reflections are indicated by red and green arrows in Figs 2(a) and (c). They are so strong that later primary reflections are masked. We use the computed 2-D reflection data set as input to solve eq. (1) for retrieving R_t with $m = 1, ..., 10$. Two of the corresponding retrieved data sets are shown in Figs 2(b) and (d). Note that internal multiple reflections, indicated by the red and green arrows in Figs 2(a) and (c), are absent and later primary reflections are recovered in Figs 2(b) and (d).

We use the velocity model shown in Fig. 1(b) for migrating the computed and retrieved data sets. A one-way wave equation migration scheme is used here. The computed images of the target zone are shown in Figs 3(a) and (b). The image shown in Fig. 3(a) is from the computed data set and contains artefacts arising from internal multiple reflections, indicated by the red arrows, because of the single-scattering assumption of the migration scheme. The image shown in Fig. 3(b), which is from the retrieved data set, is free from these artefacts. Note that there are some gaps indicated by the green arrows in Figs 3(a) and (b), which are caused by the finite length of the acquisition.

Laboratory data set

The physical model shown in Fig. 1 has well-defined and well-separated interfaces and the measured data set appears to be fit enough for IME by the MME scheme. We apply the MME scheme to the selected 2-D slice of the laboratory data set to test its performance. The measured laboratory data set has been pre-processed with following steps:

(1) Mute direct wave.
(2) Interpolate the missing near-offset data using parabolic Radon transform (Kabir & Verschuur 1995).
(3) Multiply the data set with $\sqrt{t}$ time gain to correct from 3-D to 2-D propagation.
(4) Deconvolve source wavelet with predictive deconvolution.
(5) Interpolate receivers using sparse linear Radon transform (Trad *et al.* 2003) (random noise was also attenuated in this step because of the denoising effect of the sparse Radon transform).

Note that the ghosts and reflections from the free surface and both sides of the model fall well outside the measured time window. Thus, they are not present in the measured data set.

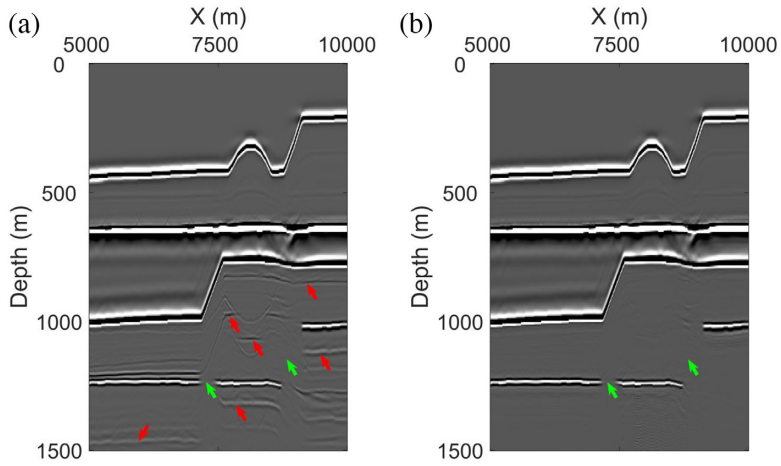

Figure 3. (a) The image retrieved from the computed data set and (b) the image retrieved from the resulting data set of the MME scheme. The red arrows in (a) indicate artefacts arising from internal multiple reflections, the green arrows in (a) and (b) indicate gaps in the image.

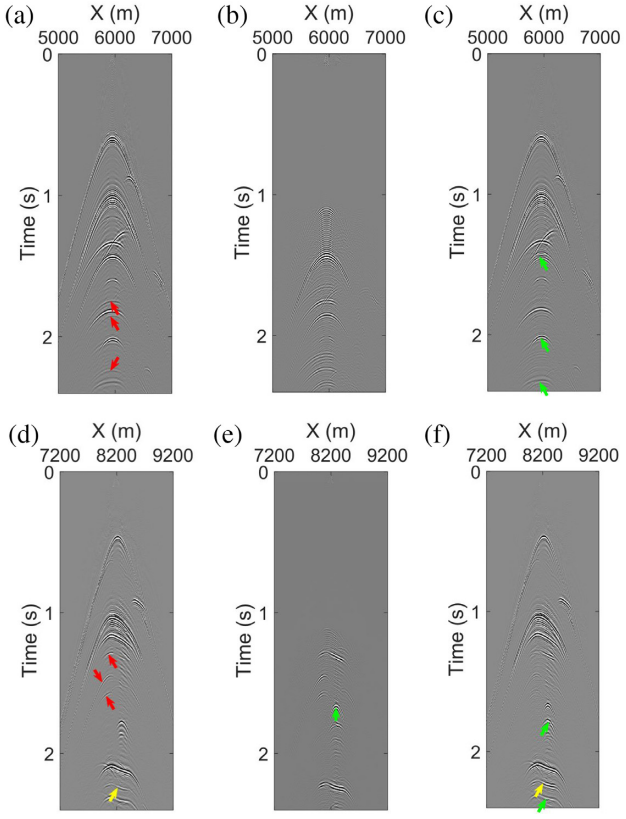

Figure 4. Two processed reflection responses from the 2-D slice of the laboratory data set are shown for source positions at 6000 m (a) and 8200 m (d) as indicated by the red arrows in Fig. 1(b), the corresponding predicted internal multiple reflections are shown in (b) and (e); (c) and (f) show the multiple-eliminated reflection responses. The red and green arrows indicate internal multiple reflections. The yellow arrows indicate the internal multiple reflection that becomes stronger after the processing by MME.

Two reflection responses with source positions indicated by the red arrows in Fig. 1(b) are shown in Figs 4(a) and (d). We use the selected line data set as input to solve eq. (1) for retrieving R_t with $m = 1, \ldots, 6$ (more iterations would cause smearing in the data because of the low quality of the pre-processed data set). The predicted internal multiple reflections are given in Figs 4(b) and (e), and the corresponding retrieved data set are shown in Figs 4(c) and (f). Internal multiple reflections indicated by the red, yellow and green arrows are analysed in the Discussion section.

We use the velocity model shown in Fig. 1(b) for migrating the measured and retrieved line data sets. The same migration scheme is used here as in the numerical data set. The migration images of the target zone are shown in Figs 5(a) and (b). We can see that artefacts due to internal multiple reflections indicated by red arrows in Fig. 5(a) are absent in Fig. 5(b), which is from the retrieved data set. However, the artefact indicated by the green arrow in Fig. 5(a) becomes stronger in Fig. 5(b). Gaps in Figs 5(a) and (b) are caused by the limited length of the acquisition similar to those in the modelled data set.

DISCUSSION

The application of the MME scheme to the computed reflection responses shows that it has excellent performance; all orders of internal multiple reflections are successfully removed as shown in Fig. 2. The migration image given in Fig. 3(b) shows that the structure of the model can be imaged from the resulting data set of the MME scheme without artefacts arising from internal multiple reflections. This validates the MME scheme for a numerical model. No model information or adaptive subtraction is used in the implementation.

The MME scheme successfully predicts all orders of internal multiple reflections in the measured data set as shown in Figs 4(b) and (e). The resulting R_t retrieved from eq. (1), shown in Figs 4(c) and (f), show that some of the internal multiple reflections are successfully removed. The events indicated by the red arrows in Figs 4(a) and (d) are absent in Figs 4(c) and (f). The related artefacts in the migration image have disappeared as shown in Fig. 5. However, some internal multiple reflections are still visible in Figs 4(c) and (f), such as events indicated by the green and yellow arrows in Figs 4(c) and (f). This is caused by the amplitude mismatches of these events. In order to investigate the causes of amplitude mismatches, we study the effect of possible attenuation in the model that is not accounted for by the MME scheme. We use $Q = 20$ in the model shown in Figs 1(b) and (c) to mimic attenuation in the medium. The same measurements and source wavelet are used here as in the numerical 2-D data set and the computed shot gather with source position at 8200 m is given in Fig. 6(a). Internal multiple reflections present in Fig. 2(c) are still present in Fig. 6(a) (indicated by red and green

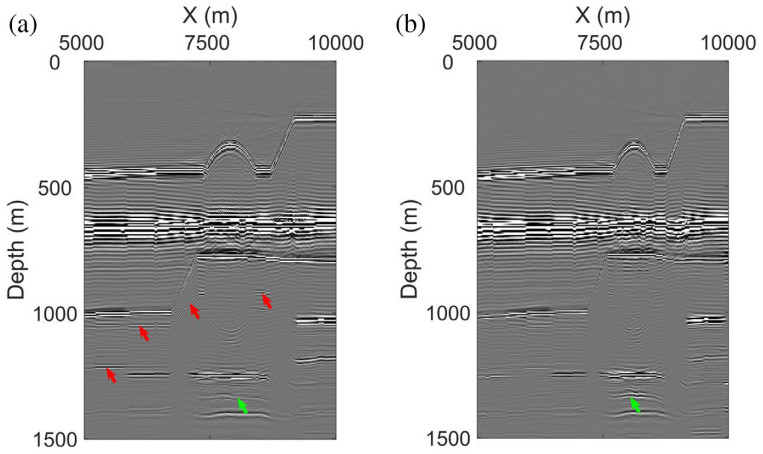

Figure 5. (a) The image from the 2-D slice of the laboratory data set and (b) the image from the resulting data set of the MME scheme. The red and green arrows in (a) indicate artefacts arising from internal multiple reflections and the green arrow in (b) indicates the artefact that has become stronger than the artefact in the image of the data.

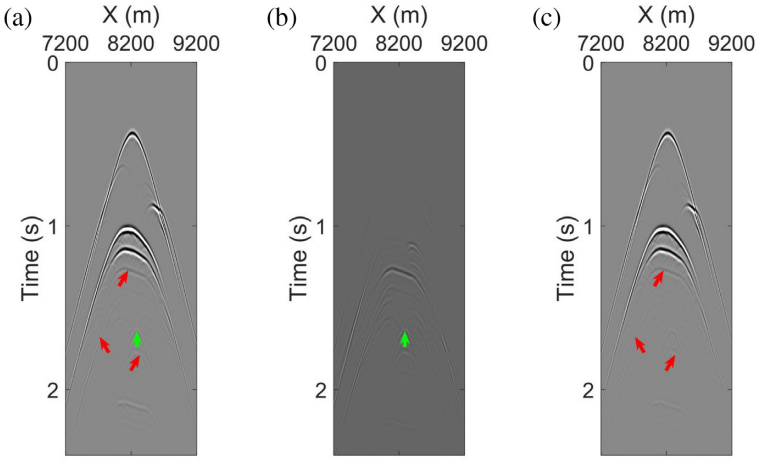

Figure 6. (a) The computed reflection response from the dissipative medium and (b) the predicted internal multiple reflections by the MME scheme. (c) The multiple eliminated data. The red and green arrows in (a)–(c) indicate internal multiple reflections.

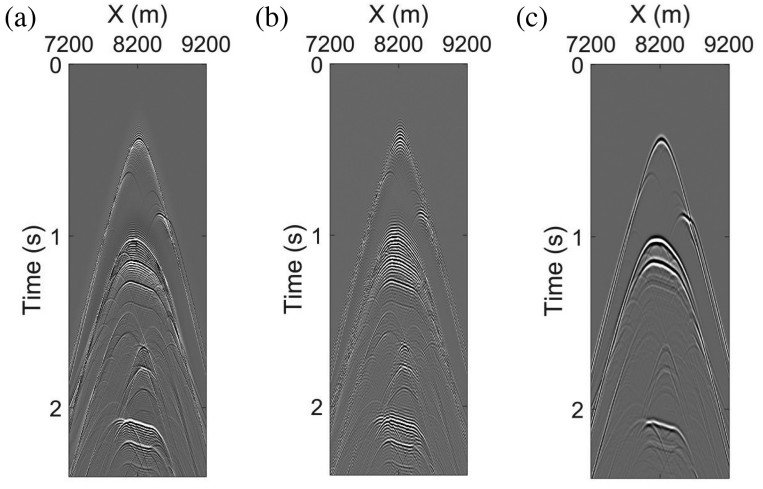

Figure 7. (a) The computed flat frequency data and (b) the wavelet deconvolved data. (c) The multiple eliminated data.

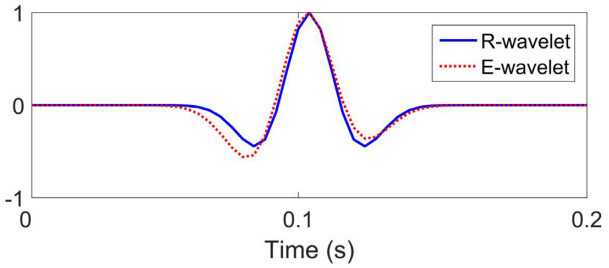

Figure 8. The comparison of the actual source wavelet (R-wavelet) and the estimated source wavelet (E-wavelet) used for the source wavelet deconvolution.

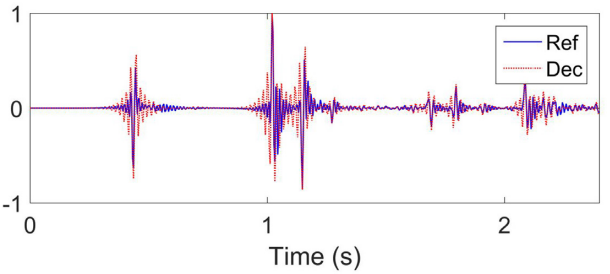

Figure 9. The comparison of zero-offset traces from the computed flat frequency data (Ref) shown in Fig. 7(a) and the wavelet deconvolved data (Dec) shown in Fig. 7(b).

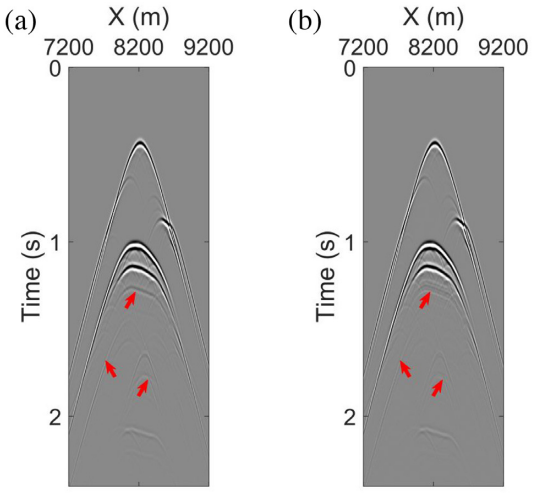

Figure 10. (a) The computed reflection response from the dissipative medium and (b) the multiple eliminated data.

arrows) but weaker. The predicted internal multiple reflections by the MME scheme is shown in Fig. 6(b). Similar to the lossless case, all internal multiple reflections are successfully predicted. However, the shot gather after multiple elimination given in Fig. 6(c) shows that the residuals of internal multiple reflections are still there. This is caused by the fact that the predicted internal multiple reflections have lower amplitudes than the actual ones in the measured data set because of the attenuation. The experiment validates that attenuation is one factor to result in the presence of remnant internal multiple reflections in the resulting data set of the MME scheme.

Imperfect source wavelet estimation is another well-known factor to cause the amplitude mismatches and we use the computed numerical 2-D lossless data set to analyse this effect. Fig. 7(a) gives a computed flat frequency shot gather with source position at 8200 m, which is used as a reference to illustrate the effect of the imperfect source wavelet estimation. The wavelet indicated by the red dashed line in Fig. 8 is used as the estimated source wavelet for the deconvolution. The estimated wavelet is an 18 Hz Ricker wavelet with distorted phase to mimic the field case and the actual wavelet used for computing the data set is a 20 Hz Ricker wavelet indicated by the blue line in Fig. 8. We deconvolve the computed data set with the estimated 18 Hz Ricker wavelet to obtain the wavelet deconvolved data set. The data set after source wavelet deconvolution is given in Fig. 7(b). The zero-offset traces in Figs 7(a) and (b) are picked and put in Fig. 9 for the comparison of the amplitude information. Both traces have been normalized by the same factor. Fig. 9 shows that the imperfect estimation of source wavelet causes amplitude errors after the source wavelet deconvolution. We use the deconvolved data set as input to solve eq. (1) and the retrieved data is given in Fig. 7(c). Compared with Fig. 2(d), the residuals of multiple reflections are present in Fig. 7(c). This experiment validates that the imperfect estimation of source wavelet is another factor to cause the presence of remnant internal multiple reflections in the resulting data set.

We combine the attenuation and imperfect source wavelet estimation to go on testing their effect on amplitude information. The computed lossy data set and estimated 18 Hz Ricker wavelet are used here. The computed lossy data set is deconvolved with the estimated 18 Hz Ricker wavelet to obtain the source wavelet deconvolved data set. The computed lossy shot gather with source position at 8200 m is given in Fig. 10(a) and the corresponding retrieved data by MME is given in Fig. 10(b). It can be seen that internal multiple reflections indicated by red arrows in Fig. 10(a) are still present in Fig. 10(b) because of amplitude mismatches caused by attenuation and imperfect source wavelet estimation.

The experiments introduced above show that attenuation and imperfect source wavelet estimation cause amplitude errors and correspondingly, degrade the performance of MME for internal multiple reflection elimination. This partly explains the presence of remnant internal multiple reflections after the processing by MME in the laboratory example. Except for the attenuation and imperfect source wavelet estimation, 3-D to 2-D propagation correction also causes amplitude mismatches as discussed by Staring et al (2018) and correspondingly degrades the performance of MME. Based on the experiments and analyses, we can conclude that high-quality pre-processing is crucial for the MME scheme. Adaptive subtraction could be a possible option for the subtraction of internal multiple reflections from the measured data set when poor-quality pre-processing was performed. However, we prefer not to use it because adaptive subtraction could remove both primary and multiple reflections when they overlap.

The event indicated by the green arrow in Fig. 4(e) is the internal multiple reflection related to the first and second horizontal reflectors and is successfully predicted by the MME scheme. It is also present in the computed shot gather indicated by the green arrow in Figs 2(c) and 6(a). There it is successfully eliminated as well by the MME scheme as shown in Fig. 2(d) or attenuated as shown in Fig. 6(c). However, it is not present in the measured data shown in Fig. 4(d) but present in the retrieved data shown in Fig. 4(f). This does not necessarily mean that the MME scheme introduces a non-physical event. A possible reason can be that this event is cancelled by other events in the 3-D geometry of the laboratory model such that it is missing in the 2-D slice of the laboratory data.

From a cost perspective, the MME scheme involves ten iterations for the numerical data set and six iterations for the 2-D slice of the laboratory data set for each time instant. The computational cost

increases with the size of the data set. The MME scheme allows for a computationally less expensive implementation by using the previously computed filter functions as initial estimate for every new time instant (Zhang & Slob 2020). In this case, the computational effort is reduced by up to an order of magnitude.

CONCLUSIONS

We have applied the MME scheme to a measured laboratory data set to test the performance. No model information or adaptive subtraction is used in the implementation. The laboratory data example shows that several internal multiple reflections are successfully removed or attenuated, but some remnant multiple reflections remained. In one location a multiple was predicted that was present in the computed data but not in the measured data. It is likely that the absence of this multiple in the measured data comes from 3-D effects not captured in the 2-D model slice used for computing the 2-D data set. Given the overall successful application of the method to the laboratory data, we think the MME scheme is an appropriate method for internal multiple reflection elimination.

ACKNOWLEDGEMENTS

This work is part of the Open Technology Program with project number 13939, which is financed by NWO Domain Applied and Engineering Sciences. The numerical reflection responses in this paper are computed with the finite-difference package in Thorbecke & Draganov (2011). The authors would like to thank Eric Verschuur, Joeri Brackenhoff and Jan Thorbecke for many fruitful discussions. The Delphi consortium is acknowledged for making the laboratory data set available.

REFERENCES

Araújo, F.V., Weglein, A.B., Carvalho, P.M. & Stolt, R.H., 1994. Inverse scattering series for multiple attenuation: an example with surface and internal multiples, in *64th Annual Meeting*, SEG, Expanded Abstracts, pp. 1039–1041.

Berkhout, A.J. & Verschuur, D.J., 1997. Estimation of multiple scattering by iterative inversion, Part I: Theoretical considerations, *Geophysics,* **62,** 1586–1595.

Blacquiere, G., Volker, A.W.F. & Ongkiehong, L., 1999. 3-D physical modeling for acquisition geometry studies, in *69th Annual Meeting*, SEG, Expanded Abstracts, pp. 1212–1215.

de Melo, F.X., Idris, M., Wu, Z.J. & Kostov, C., 2014. Cascaded internal multiple attenuation with inverse scattering series, in *84th Annual Meeting*, SEG, Expanded Abstracts, pp. 4113–4117.

Jakubowicz, H., 1998. Wave equation prediction and removal of interbed multiples, in *68th Annual International Meeting*, SEG, Expanded Abstracts, pp. 1527–1530.

Kabir, M.M.N. & Verschuur, D.J., 1995, Restoration of missing offsets by parabolic Radon transform, *Geophys. Prospect.,* **43,** 347–368.

Koek, E.A., Faber, G. & Berkhout, A.J., 1995. 3-D data acquisition research with the Delft physical modeling facility, in *65th Annual Meeting*, SEG, Expanded Abstracts, pp. 747–748.

Löer, K., Curtis, A. & Meles, G.A., 2016. Relating source-receiver interferometry to an inverse-scattering series to derive a new method to estimate internal multiples, *Geophysics,* **81**(3), Q27–Q40.

Luo, Y., Kelamis, P.G., Huo, S., Sindi, G., Hsu, S. & Weglein, A.B., 2011. Elimination of land internal multiples based on the inverse scattering series, *Leading Edge,* **30,** 884–889.

Matson, K., Corrigan, D., Weglein, A., Young, C. & Carvalho, P., 1999. Inverse scattering internal multiple attenuation: Results from complex synthetic and field data examples, in *89th Annual Meeting*, SEG, Expanded Abstracts, pp. 1060–1063.

Staring, M., van der Neut, J. & Wapenaar, K., 2018. Marchenko redatuming by adaptive double-focusing on 2D and 3D field data of the Santos basin, in *88th Annual Meeting*, SEG, Expanded Abstracts, 5449–5453.

Ten Kroode, P.E., 2002. Prediction of internal multiples, *Wave Motion,* **35,** 315–338.

Thorbecke, J. & Draganov, D., 2011. Finite-difference modeling experiments for seismic interferometry, *Geophysics,* **76**(6), H1–H18.

Trad, D., Ulrych, T. & Sacchi, M., 2003. Latest views of the sparse Radon transform, *Geophysics,* **68**(1), 386–399.

van der Neut, J. & Wapenaar, K., 2016. Adaptive overburden elimination with the multidimensional Marchenko equation, *Geophysics,* **81**(5), T265–T284.

van Groenestijn, G.J.A. & Verschuur, D.J., 2009. Estimating primaries by sparse inversion and application to near-offset data reconstruction, *Geophysics,* **74**(3), A23–A28.

Verschuur, D., Berkhout, A. & Wapenaar, K., 1992. Adaptive surface-related multiple elimination, *Geophysics,* **57,** 1166–1177.

Wapenaar, K., Brackenhoff, J., Thorbecke, J., van der Neut, J., Slob, E & Verschuur, E., 2018. Virtual acoustics in inhomogeneous media with single-sided access, *Sci. Rep.,* **8,** doi:10.1038/s41598-018-20924-x.

Weglein, A.B., Gasparotto, F.A., Carvalho, P.M. & Stolt, R.H., 1997. An inverse scattering series method for attenuating multiples in seismic reflection data, *Geophysics,* **62,** 1975–1989.

Zhang, L. & Slob, E., 2019. Free-surface and internal multiple elimination in one step without adaptive subtraction, *Geophysics,* **84**(1), A7–A11.

Zhang, L. & Slob, E., 2020. Implementation of a fast algorithm for multiple elimination and transmission compensation in primary reflections, *Geophys. J. Int.,* **221,** 371–377.

Zhang, L. & Staring, M., 2018. Marchenko scheme based internal multiple reflection elimination in acoustic wavefield, *J. Appl. Geophys.,* **159,** 429–433.

Zhang, L., Slob, E., van der Neut, J. & Wapenaar, K., 2018. Artifact-free reverse time migration, *Geophysics,* **83**(5), A65–A68.

Zhang, L., Thorbecke, J., Wapenaar, K. & Slob, E., 2019a. Transmission compensated primary reflection retrieval in data domain and consequences for imaging, *Geophysics,* **84**(4), Q27–Q36.

Zhang, L., Thorbecke, J., Wapenaar, K. & Slob, E., 2019b. Data-driven internal multiple elimination and its consequences for imaging: a comparison of strategies, *Geophysics,* **84**(5), S365–S372.